Research Square

Preprints are preliminary reports that have not undergone peer review.
They should not be considered conclusive, used to inform clinical practice,
or referenced by the media as validated information.

Stress alleviation via FCC-twinning in additively manufactured alloy

Zechen Fang
China Astronaut Research and Training Center
Zhi-Lin Wu
wuruinan-1994@njust.edu.cn

Nanjing University of Science and Technology
Lei Zhao
Nanjing University of Science and Technology
Chen-Guang Huang
Chinese Academy of Sciences
Chen-Wu Wu
cwwu@csu.ac.cn

Chinese Academy of Sciences

Research Article

Keywords:

Posted Date: November 26th, 2026

DOI: https://doi.org/10.21203/rs.3.rs-11827083/v1

License: This work is licensed under a Creative Commons Attribution 4.0 International License.
Read Full License

Additional Declarations: The authors declare no competing interests.

Stress alleviation via FCC-twinning in additively manufactured alloy

Ze-Chen Fang[1], Zhi-Lin Wu[2, *], Lei Zhao[2], Chen-Guang Huang[3] and Chen-Wu Wu[3, *]

[1]*China Astronaut Research and Training Center, Beijing 100094, China*
[2]*School of Mechanical Engineering, Nanjing University of Science and Technology, Nanjing 210094, China*
[3]*CAS Key Laboratory of Space Manufacturing Technology, Technology and Engineering Center for Space Utilization, Chinese Academy of Sciences, Beijing 100094, China*

ABSTRACT.
Selective Laser Melting (SLM) process inevitably introduces residual stresses, which could be alleviated largely by multi-layer scanning thermal cycling. Such alleviation is found to be originated from the directional growth of the α" columnar precipitates, while the continuous FCC-twinning structures multiply and are segmented into subgrains by sheared pyramidal stacking faults. The successive extended partial dislocations react at the junction of basal and pyramidal stacking faults outside FCC-twinning subgrains to form a Basal-Pyramidal (B–P) lock configuration. Such subgrain pattern is driven by the evolution of dislocations and stacking faults alongside continuous stress fluctuations underpinning the stress relief, which has been verified via molecular dynamics simulations and in situ characterization.

I. INTRODUCTION.

The rapid heating and cooling cycles inherent in SLM process inevitably introduce sophisticated residual stress fields into the as-built alloy parts, which adversely reduce the formation rate, the performance and durability [1] The rapid directional movement of the laser spot induces unbalanced primary stress and microstructures. Subsequently, multiple thermal cycling brings about prominent alterations to the microstructure and mechanical responses of deposited layers.

It was found that SLM-fabricated titanium specimens exhibit obvious microstructural anisotropy [2]. Similarly, with directional heat transfer continuously changing dynamically in laser processing, thermal cycling characteristics and the parametric dependency of residual stress (RS) also change accordingly [3]. The parameter dependence of residual stress under multi-layer scanning thermal cycling has been verified through experimental and numerical results [3]. It can be seen from Fig. 1(a) that residual stress (RS) drops significantly with the increase in laser energy density under multi-layer scanning thermal cycling. Further metallurgical characterization of crystalline phases reveals that this effect coincides with the rising density of directionally grown columnar α" variants in Fig. 1(c). This unique microstructural observation deserves in-depth investigation. Controlling residual stress to improve the structural integrity of SLM-ed components hinges on uncovering microscale evolution mechanisms [4-6]. Laser-induced nanotwinning and other defect engineering driven by phase transformation offer innovative strategies for designing high-performance alloys [7]. For instance, the existence of the FCC phase can significantly increase the local yield strength of the sample [8]. It has also been proved that nanotwinned FCC phases can significantly enhance the strength of the material [9, 10].

The present study probes microstructural evolution during the directional growth of characteristic α" columnar grains under multi-layer scanning thermal cycling, to elucidate the intrinsic mechanisms of residual stress variations. To address the above challenge, large-scale molecular dynamics (MD) simulations are utilized to realize synchronous thermal-stress-deformation coupling at the atomic scale. This approach also enables full characterization of phase transformation, nucleation, grain growth, as well as typical microdefects such as twin boundaries, dislocations and stacking faults [11, 12]. Combined with crystallographic analysis results, the directional growth model of characteristic columnar α" grains was constructed in this work. The microstructural mechanism of RS induced by high-energy multi-layer scanning thermal cycling was investigated as follow.

II. METHODOLOGY

To characterize energy transport in SLM processing, we developed a two-temperature MD model in our earlier work [12], as shown in Fig. 1(b). Simulation outputs demonstrate that powder deposition interfaces exhibit markedly higher electron–phonon coupling efficiency than internal powder regions. This performance discrepancy originates from heterogeneous electron density distributions induced by multi-layer laser scanning. These interfaces absorb more laser-derived electronic energy, thereby promoting the remelting of crystalline metallic materials within the underlying deposited layer. At the later solidification stage, heat dissipation from the upper melt pool and the underlying deposited layer yields peak cooling rates at the interface, hence generating an upward directional solidification front in

*Contact author: wuruinan-1994@njust.edu.cn,
*Contact author: cwwu@csu.ac.cn

the overlying molten metal. To sum up, the intrinsic thermal features of multi-layer scanning thermal cycling are interfacial heat transfer and unidirectional temperature gradients, which share identical characteristics with traditional directional solidification: fixed substrate, unidirectional heat dissipation, and preferential grain growth. Solidification under multi-layer thermal cycling is essentially a continuous dynamic directional solidification process.

Cyclic thermal loading induced by multi-layer laser scanning on the deposited region causes local remelting and displacive transformation of the basket-weave α+β microstructure [13]. Partial α' martensite undergoes secondary dynamic recrystallization, generating short columnar α" martensite preferentially oriented along the build direction <0001>. As shown in Fig. 1, high-energy multi-layer scanning thermal cycling increase the distribution density of α" phase, accompanied by a substantial reduction in thermal stress. Hence, an in-depth investigation of the intrinsic properties of these featured grains is warranted.

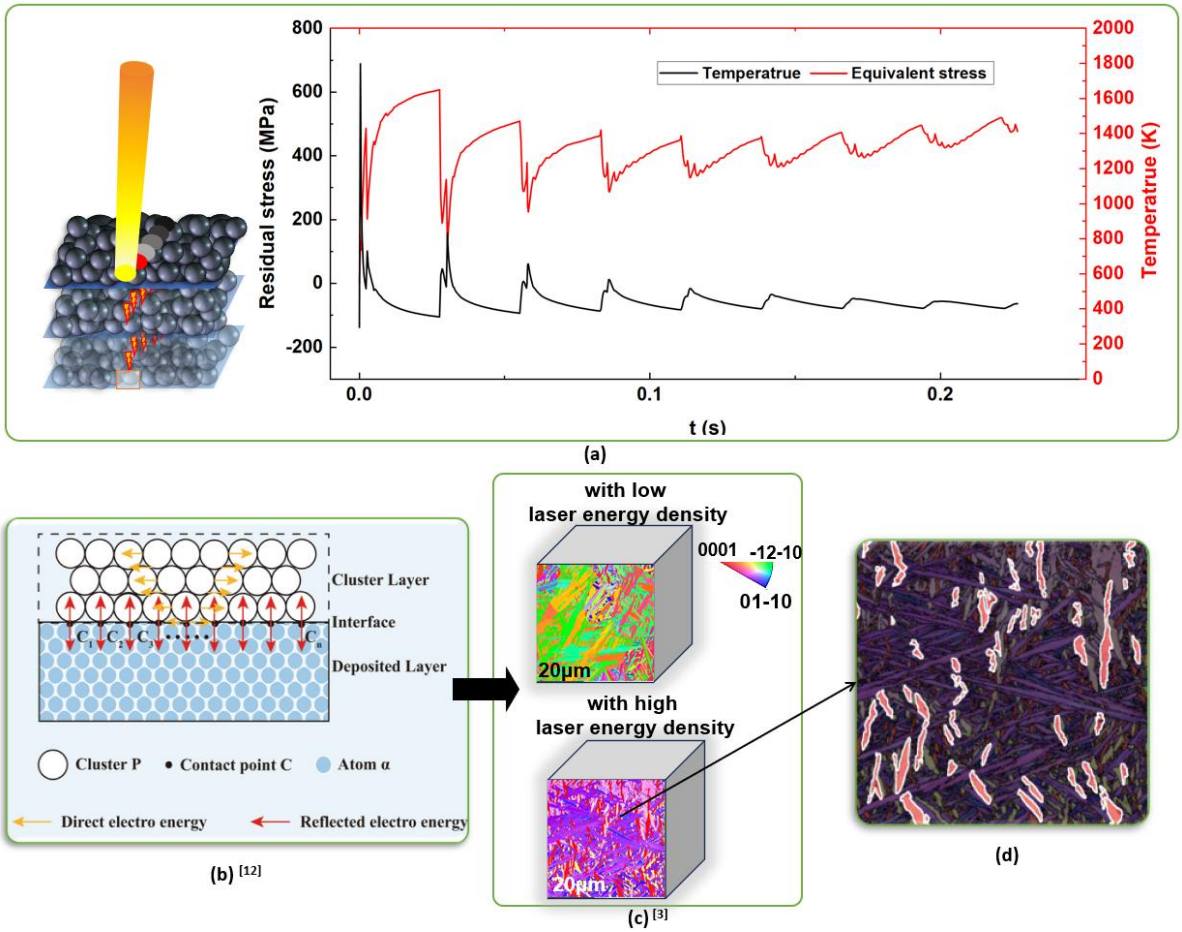

FIG 1. Multiphysics characteristics under thermal cycles of multi-layer scanning: (a) stress varies negatively with temperature during multi-layer scanning thermal cycles; (b) efficient interfacial energy coupling and bidirectional heat dissipation induce interfacial temperature gradients and solidification fronts; (c) increasing the energy density of multi-layer scanning thermal cycles significantly raises the distribution density of columnar α" phase; (d) morphological details of columnar α" phase.

Based on the above analyses and findings, the directional solidification model was adopted to simulate solidification of the characteristic columnar α" grain during multi-layer scanning thermal cycling. The deposited layer serves as a cold substrate and seed crystal; the newly formed melt pool acts as the liquid metal phase; and the dense deposit with high heat capacity enables efficient interfacial heat transfer, which functions as forced unidirectional heat dissipation. Meanwhile, the lattice orientations of seed crystals in the model are provided by the preferred orientation of columnar α" precipitates characterized via EBSD analysis. Fig. 2 shows the schematic of the present model. The orientation of the short columnar α" phase was set to <-2110> along the x-direction, <01-10> along the y-direction, and <0001> along the

z-direction, obtained from crystallographic analysis performed in Oxford AZtecCrystal software. The seed crystal is arranged at the bottom of the model. The overlying molten titanium is induced by the seed crystal to crystallize and grow along the building direction <0001>, which vividly demonstrates the entire process whereby α" variants directionally solidify under the high energy input of multi-layer scanning thermal cycling.

Molecular dynamics simulations were performed using LAMMPS. The simulation dimension was set to 10nm×10nm×25nm with 144000 Ti atoms. Interatomic interactions were described using an EAM/FS (Finnis–Sinclair) potential, which accurately reproduces high-temperature phase behaviors of titanium during melting and ultrafast non-equilibrium solidification. The initial structure was relaxed through conjugate gradient energy minimization, after which atomic velocities were assigned according to the Maxwell–Gaussian distribution at 300 K. Atoms at the bottom layer were fixed to prevent lattice drift and stabilize the solidification front. A three-step scheme of heating, isothermal melting and rapid cooling was applied, with sequential NPT and NVT ensemble control. The system was fully relaxed and melted at 2500K under NPT to eliminate structural memory and relax pressure. Upon molten equilibrium, the ensemble was switched to NVT, and the system was cooled linearly from 2500 K to 300 K at 1.1 K/ps to reproduce ultrafast directional solidification. Starting from the phonon-energy equation of the two-temperature model, we establish a microscale–macroscale scaling relation based on the phonon thermal diffusivity and the corresponding characteristic diffusion velocity, and examine the timescales of melting and solidification using the interfacial energy balance. This analysis provides a cooling-rate calibration for microscale simulations of selective laser melting (SLM); detailed derivations are given in Appendices A–D. The constant-volume quenching scheme captures the inertial confinement features of molten pool in additive manufacturing during ultrafast solidification, where rigid external constraints suppress free volume relaxation. This approach conforms to actual high-cooling-rate processing conditions, highlights the directional nucleation guidance of the underlying seed crystal, recovers the epitaxial growth behavior of liquid microstructures on the substrate, and precisely captures the characteristics of extreme non-equilibrium solidification of titanium materials in additive manufacturing.

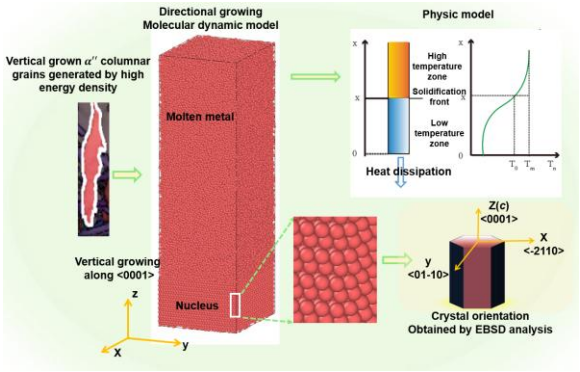

FIG. 2 The molecule dynamic model of columnar α' grain in the process of directional solidification.

III. RESULTS

The microstructure evolution during the directional growth of α" columnar crystals is shown in Fig. 3, in which grain nucleation and growth start from the {0001} crystal planes adjacent to the seed crystal, accompanied by the formation of twins, dislocations, and stacking faults. Notably, the close-packed {111} planes of the FCC structure act as twin boundaries. The crystallographic orientation of the FCC phase, extracted via polyhedral template matching (PTM) from molecular dynamics (MD) simulations, was determined to be $(32\bar{2})_{\mathrm{FCC}}[2\bar{1}2]_{\mathrm{FCC}}$. Its orientation relationship with the matrix α-HCP phase obeys the classic Burgers orientation relationship (BOR) for titanium alloys: $(0001)_{\alpha'} \parallel \{111\}_{\mathrm{FCC}}$ and $\langle 11\bar{2}0\rangle_{\alpha'} \parallel \langle 1\bar{1}0\rangle_{\mathrm{FCC}}$ [8, 9]. It has been reported that FCC-structured titanium is commonly found alongside coherent twin boundaries [14].

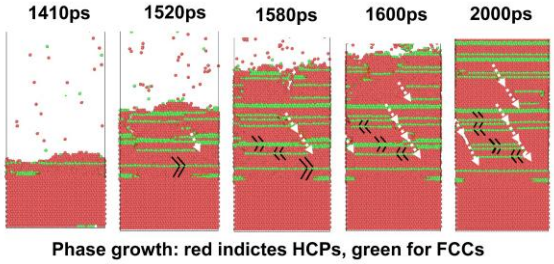

FIG. 3. Phases evolution in the directional growth of α"column crystals.

Fig. 4 illustrates the formation mechanism of continuous twins and FCC nano-bands during the growth process. At the solidification front, FCC phase forms via ledge growth. The newly nucleated HCP phase above the FCC interface slips by 1.5b relative to the underlying HCP matrix along the <01-10> partial slip vector. Resembling the formation of stacking fault twins, ABC-stacked twins bounded by coherent twin boundaries formed by FCC close-packed planes continuously nucleate and propagate in both horizontal and vertical directions along with the

directional growth of the crystal. Above observations indicate continuously expanding stacking fault twins form during grain growth. The significant thermal gradients and cyclic thermal loads inherent to the selective laser melting (SLM) process directly promotes the formation and stabilization of this FCC twinning structure [8].

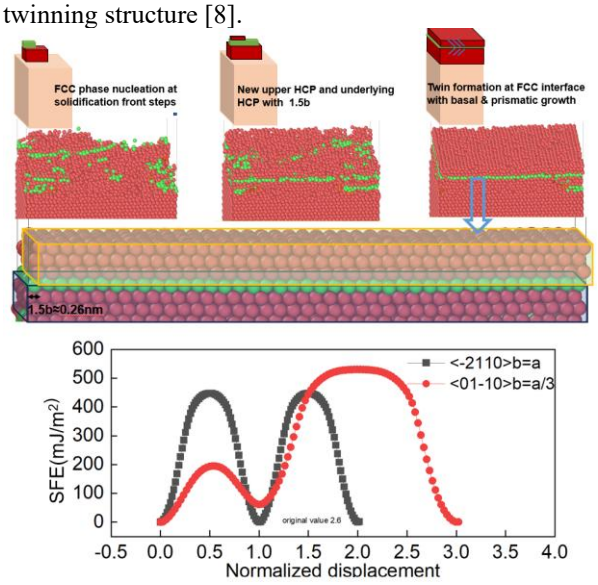

FIG. 4. Evolution mechanism of stacking fault twinning during grain growth.

Reducing basal stacking fault energy (SFE) can promote the generation of abundant basal stacking faults (BSFs) and FCC nanobands [15]. To clarify the specific mechanism of SFE during directional growth, basal slip stacking fault simulations along <01-10> and <-2110> were carried out on this structure. GSFE curves in Fig. 4 show the unstable stacking fault energy of <01-10> is merely ~200 mJ/m² at early slip stages, much lower than the energy barrier of <-2110>, meaning that Shockley partial dislocations along <01-10> activate readily with low nucleation resistance for intrinsic stacking faults. At normalized slip u=1.0, the curve reaches a stable energy minimum and produces thermodynamically stable intrinsic stacking faults, which act as precursors for twinning. By contrast, full <-2110> slip retains a high energy of ~450 mJ/m² at u=1.0 without stable stacking faults. Its high barrier only allows temporary elastic slip, incapable of preserving stable defects or inducing stacking faults and twinning plasticity. Owing to the combined effect of low c/a ratio of α-Ti and orthogonal periodic boundaries, <01-10> slip has no conventional extrinsic stacking fault valley at u=2.0 but forms a wide metastable energy plateau ranging from u=1.5 to 2.5. This plateau arises from coexisting energy-degenerate twin transition configurations. Such metastable structures expand the energy range for twinning and provide a continuous path for twin nucleation. Accordingly, <01-10> features low-barrier intrinsic stacking fault nucleation and viable twinning evolution, while full <-2110> slip cannot generate stacking faults or twins. During directional growth, <01-10> partial slip activates preferentially, and stacking-fault twinning develops via intrinsic stacking fault evolution and deformation twin nucleation.

During ultrafast directional solidification, rapid cooling limits atomic ordering at the solid-liquid interface, producing basal stacking faults with FCC-type ABC stacking in two forms: full coverage across the basal plane and localized flake-like domains. As shown in Fig. 5, pairs of Shockley partial dislocations (Burgers vectors: 1/3<1-100>, 1/3<10-10>、1/3<01-10>) form spontaneously at the boundaries of localized faults during crystallization, constructing typical extended dislocation units where two partials sandwich a stacking fault.

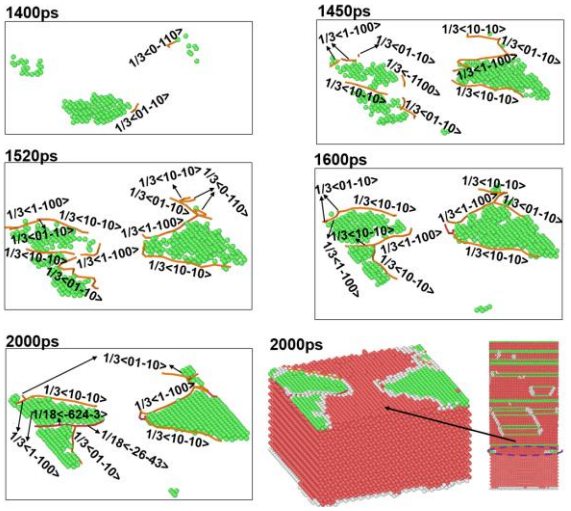

FIG. 5. Formation of extended dislocations with stacking faults confined by paired Shockley partials.

Fig. 6 illustrates the evolution of dislocation configurations during the directional crystal growth. Sequential activation of basal and prismatic slip systems throughout crystal growth induces shear slip and torsional distortion of the crystal. In the early stage of grain growth, only basal slip is activated, and the crystal interior solely contains three types of pure a-type basal Shockley partial dislocations: $\frac{1}{3}\langle 1\bar{1}00\rangle$, $\frac{1}{3}\langle 0\bar{1}10\rangle$ and $\frac{1}{3}\langle 10\bar{1}0\rangle$, which generate horizontal stacking faults parallel to the basal plane. Atomic misarrangements arising from basal slip produce continuous lamellar FCC twinning structures, consistent with the continuous twins observed in columnar grains fabricated via selective laser melting (SLM) [3].

As grain growth proceeds, the distortional stress along the c-axis accumulates persistently within the lattice.

Stable basal stacking fault configurations cannot persist for extended periods, and α-type Shockley partial dislocations readily deflect onto pyramidal planes [16]. The c-axis strain cannot be relieved by basal slip alone, thereby activating the $\{10\bar{1}1\}$ pyramidal slip system. As displayed in Fig. 6(a), various basal partial dislocations glide to the common a-type intersection lines between the basal plane and pyramidal plane, where they bend across slip planes and extend along both the basal plane and inclined pyramidal plane, respectively.

As shown in Fig. 6(b), abundant bent basal partials converge at the nodes of intersection lines and induce severe stress concentration. After overcoming the energy barrier for dislocation reactions, a+c-type pyramidal Shockley partial dislocations such as $\frac{1}{18}\langle 44\bar{6}3\rangle$ and $\frac{1}{18}\langle \bar{2}64\bar{3}\rangle$ precipitate in situ. The newly generated pyramidal partials intersect with basal partial dislocations, then separate and propagate inward into the grain. Fixed relative shear develops between the upper and lower atomic layers swept by the directional shear motion, forming early inclined pyramidal stacking faults.

When grain growth nears completion, homogenization of lattice stress drives the reconstruction of defect systems toward a low-energy steady state. The high-energy, metastable $\frac{1}{18}\langle 44\bar{6}3\rangle$ and $\frac{1}{18}\langle 20\bar{2}3\rangle$ pyramidal partial dislocations generated in the earlier stage gradually annihilate. Only the lower-energy 1/18-series partials with better compatibility with the $\{10\bar{1}1$ slip systems, including $\frac{1}{18}\langle \bar{4}043\rangle$, $\frac{1}{18}\langle 40\bar{4}3\rangle$ and $\frac{1}{18}\langle \bar{2}64\bar{3}\rangle$, are preferentially retained at the boundaries of pyramidal stacking faults. Sustained glide of pyramidal partial dislocations along pyramidal planes induces atomic stacking misarrangements, eventually yielding stable inclined pyramidal stacking faults. The aggregated basal Shockley partials are released from stress constraints and produce a small amount of perfect a-type full dislocations such as $\frac{1}{3}\langle 2\bar{1}\bar{1}0\rangle$ and $\frac{1}{3}\langle \bar{2}110\rangle$ via new dislocation combination reactions. Carrying local screw components, these full dislocations exhibit low glide resistance. Fig. 6(c) shows that they can traverse stacking fault ledges to connect defect domains on basal and pyramidal planes, efficiently dissipating residual shear strain inside grains and reducing lattice distortion energy.

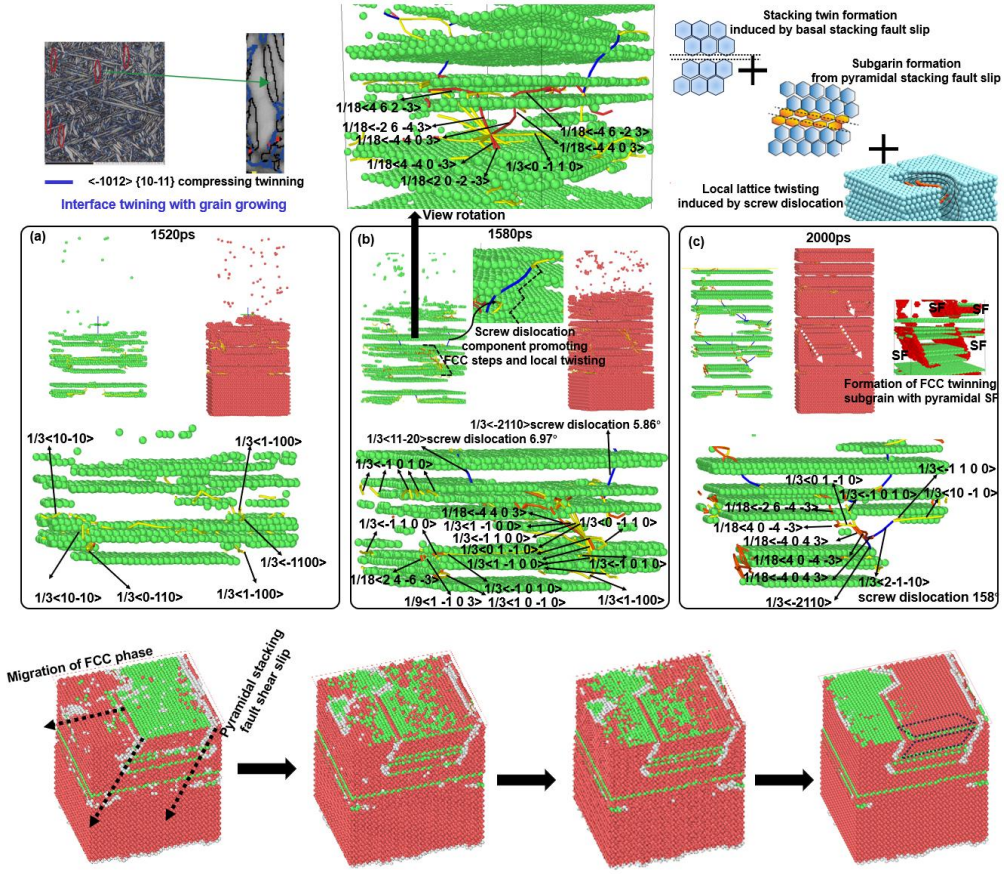

FIG. 6. The evolution of dislocation and deformation mechanism observed from the directional crystal growth.

Ultimately, under the combined action of basal partials, pyramidal partials and newly formed full dislocations, a complex defect architecture is constructed, where inclined pyramidal stacking faults intersect obliquely and basal stacking faults interpenetrate horizontally. The pyramidal stacking faults partition the FCC twin structures to form subgrains. Driven by dislocation propagation, these subgrains continuously glide obliquely downward, and their internal FCC phases migrate to adjacent basal regions during gliding as illustrated in Fig. 6. Outcrops of screw dislocations on smooth interfaces generate ledges on crystal surfaces and facilitate the accumulation of liquid-phase atoms at such ledge sites. It can be observed in Fig. 6 that inclined screw dislocation components alternately glide obliquely upward, leaving staggered ledge arrays. These ledges promote continuous generation of FCC nano-bands and basal stacking faults (BSFs), and induce localized lattice torsion. Nucleation of FCC nano-bands at twin boundaries effectively relieves internal stress and pins interfaces, refining the plastic deformation mechanism of grains.

It can thus be concluded that the full-range evolution of dislocation configurations during the directional growth of HCP-Ti grains is collectively governed by the lattice biaxial strain accommodation mechanism and dynamic stress evolution. Stress accumulation in the early stage triggers the activation of pyramidal slip, dislocation bending and the generation of pyramidal partials, enabling coordinated deformation along two axes. In the later stage, stress relaxation induces the preferential annihilation of defects, dislocation recombination and long-range glide of perfect dislocations, accomplishing steady-state reconstruction of the defect system. The complex defect network formed by the coupling of multiple types of dislocations and stacking faults ultimately dominates the plastic deformation and lattice torsion behaviors of grains.

As is evident from Fig. 7(a), with time evolving, the dislocations continuously multiply penetrating through the structure vertically. At the FCC interfaces, they rapidly develop into dislocation loops. Notice that basal and pyramidal partial dislocations keep gliding along their respective slip planes. Under the action of Escaig stress, two leading partial dislocations originating from the basal and pyramidal planes undergo dislocation reactions at the intersection line of slip planes, generating immobile rod-shaped partial dislocations. Together with the stacking faults on both sides, dislocations form ridge-like basal-pyramidal locks (B–P locks)[17, 18], which act as pinning nodes in the circled region of Fig. 7(b). The rod dislocation serves as the central node, connected to two segments of stacking faults on the basal and pyramidal planes separately, with four Shockley partial dislocations attached to its periphery, resulting an intersecting network structure which matches the TEM observations in Fig. 7(c).

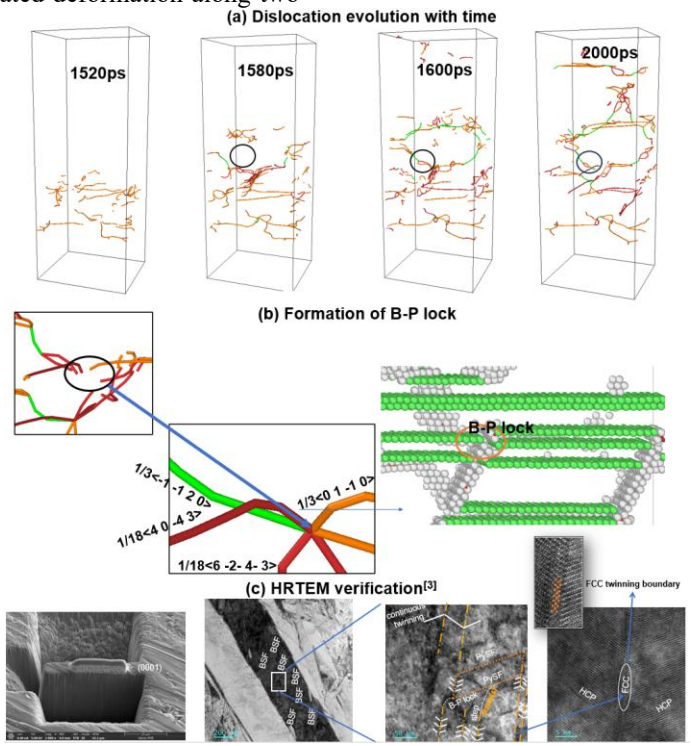

FIG. 7. The dislocation evolving with time and the formation of L-C lock.

IV. DISCUSSION

Under multi-layer scanning thermal cycling with high laser energy, FCC-type basal stacking faults are initiated via heterogeneous nucleation during the directional growth of columnar HCP grains and further evolve into stacking twins, defined herein as the FCC twinning structure. As the temperature decreases and directional growth is essentially complete, the joint slip of basal and pyramidal dislocations induces local slip and torsion within the crystal, and the FCC twinning structures are segmented into sub-grain by pyramidal stacking faults. B–P locks emerge with the propagation of partial dislocations, analogous to crack propagation in ice.

Fig. 8 illustrates the stress relief mechanism of above process. As shown in Fig. 8 (a), continuous twins result in intermixed tensile and compressive stress fields. The propagation of pyramidal stacking faults and the extension of partial dislocations provide stress redistribution pathways in these regions. As shown in Fig. 8(b)-(d), sliding and extending of pyramidal stacking fault boundaries, akin to two neighboring ice planes offsetting and pulling against each other, generates tensile deformation stress. To balance sustained boundary tensile stress, compressive stress gradually emerges within the FCC twinning subgrain. In Fig. 8(e), dislocation expansion is subjected to extrusion and damping, resembling a crack spreading in ice under compressive stress. Partial dislocations of basal and pyramidal stacking faults propagate continuously and eventually react to generate B–P locks. Once B–P locks form, dislocations under compressive stress propagate into tensile-stressed stacking faults and relieve the imbalance of tensile and compressive stresses at boundaries. This process is analogous to an ice crack expanding toward a dislocated ice layer; their connection instantaneously relaxes the prior unbalanced stress states of both domains. The above microstructural changes dissipate part of the local strain. Subgrain interiors remain in a compressive stress state in the end, while tensile stress regions along subgrain boundaries get neutralized. In this way, B–P locks interconnect multiple FCC twin subgrains in a staggered arrangement, analogous to an intersecting network formed by successive dislocated layers and cracks within ice, which forms channels for stress relaxation. Therefore, this mechanism is named "ice cracking effect".

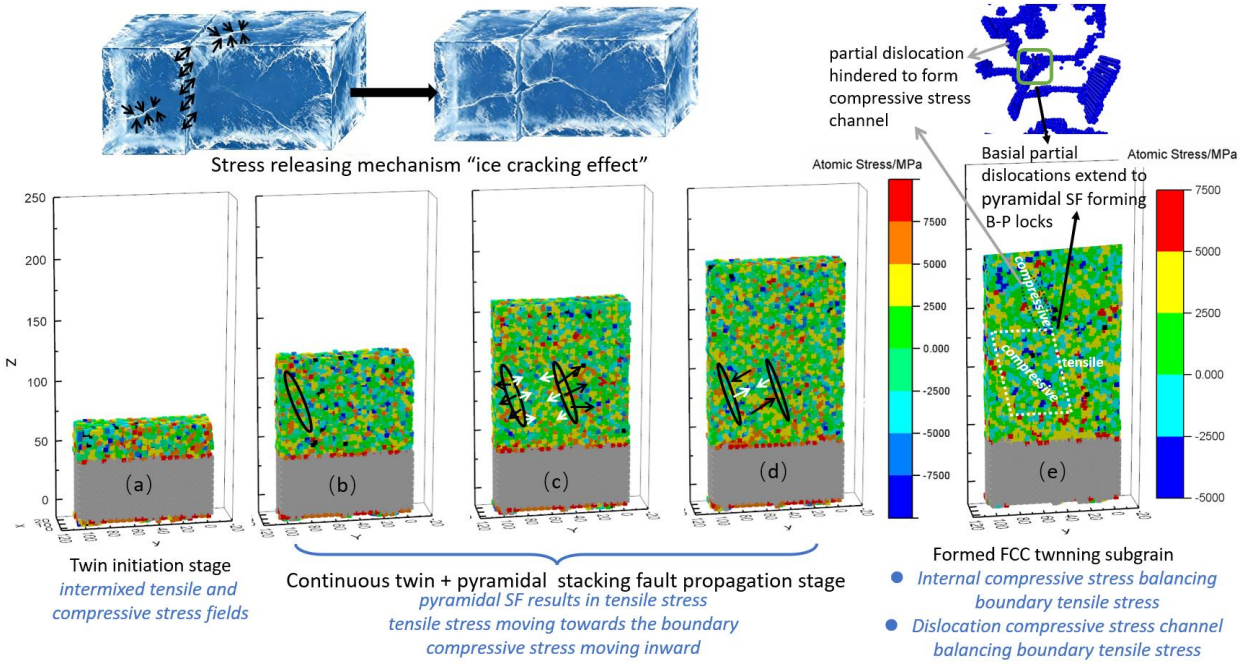

FIG. 8. Stress-relief mechanism of FCC-twinning subgrain within columnar α″ participating by high-energy-density multi-layer scanning thermal cycling in additively manufactured samples.

As FCC-twinning sub-grains network forming, the local stress/strain within α" columnar grain were effectively mitigated. After the local high stress was diluted, the mismatches would be redistributed to a wider surrounding lattice area, manifested as a decrease in peak stress at that region. Bailey–Hirsch model calculates the flow stress/yield stress increment caused by dislocation strengthening, not the residual stress in the strict sense. Nevertheless, regions with high local dislocation density produce pronounced strain associated with geometrically necessary dislocations (GNDs), which is strongly coupled with the local residual stress field. The Bailey–Hirsch model enables the quantification of the flow stress

increment contributed by GNDs. From the perspective of static spatial distribution, the flow strengthening effect in high-dislocation-density microregions is highly coupled with the local residual stress field, with consistent distribution patterns. Based on the EBSD data from the SLM-ed samples, the contours of the kernel average misorientation (KAM) and flow stress calculated by Bailey-Hirsch model were depicted in Fig. 9. The residual stress level within columnar α″ precipitates is far lower than that in other regions, which further verifies the aforementioned conclusion. The quantitative characterization of type III intragranular residual stress, particularly for dislocation-rich fine-grained specimens, represents a promising research frontier worthy of in-depth exploration in this field

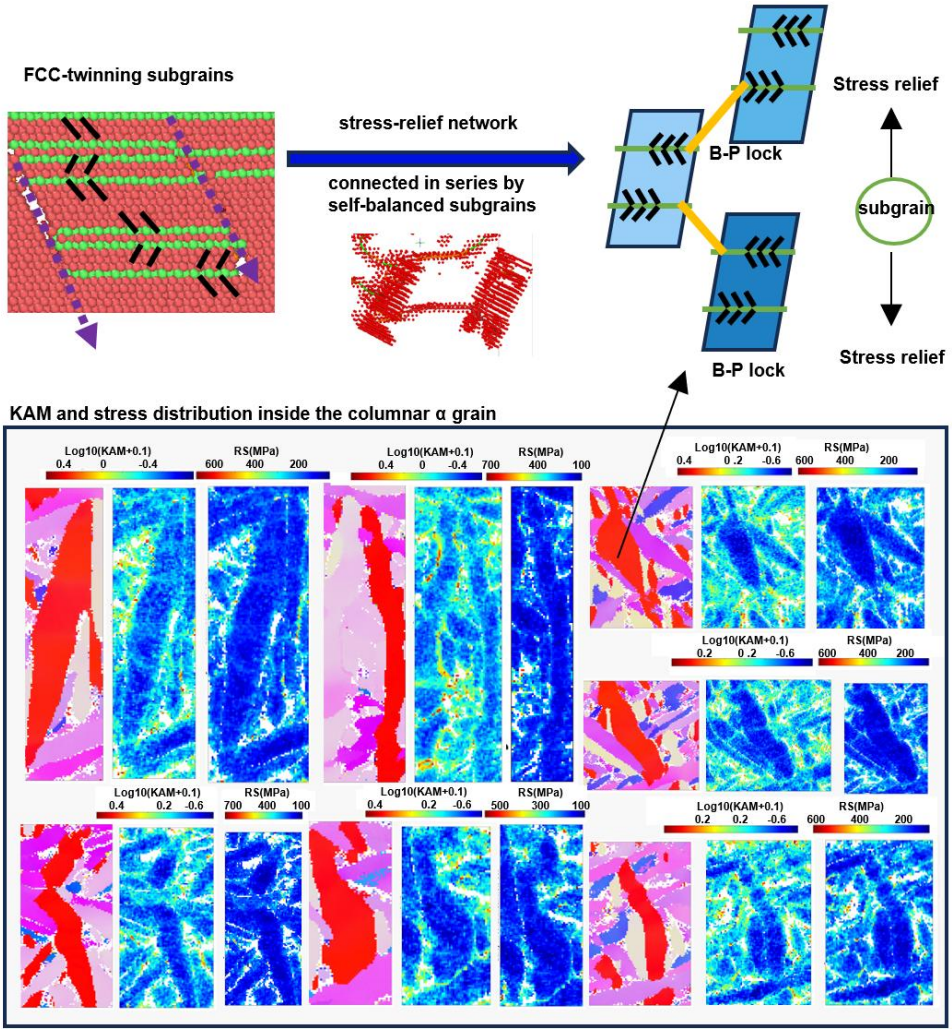

FIG. 9. Stress relief performance of FCC twinning in experimental specimens: KAM and flow stress.

V. CONCLUSIONS

The contributions of the growth of characteristic columnar α" grains and the formation of FCC twinning microstructures within the α" phase to stress relief with multi-layer scanning thermal cycling is clarified in additive manufacturing of Selective Laser Melting.

Under the thermal cycling via multi-layer laser scanning with high energy density, the α" phase precipitates and grows directionally. It is accompanied with twin proliferation and stacking faults, and ultimately results in the multiple lamellar FCC twinning microstructures. The multi FCC-twinning subgrains connected by the B-P locks form a structurally stable and stress-balanced FCC twinning microstructure network, which effectively reduces the global stress magnitudes inside the directionally grown columnar grains by the ice-cracking-like effect. The denser FCC-twinning structures can release local stress/strain concentrations significantly, which could be the very underlying mechanism on the stress relief in the deposited layer by improving the laser energy density during multi-layer thermal cycling. It might

provide a new concept for the realization of high-performance titanium alloys via additive manufacturing.

ACKNOWLEDGMENTS

We acknowledge funding from the National Natural Science Foundation of China (Grant No.11572327).

APPENDIX A: THE PHONON-ENERGY EQUATION DEFINES THE TRANSPORT PARAMETER

The standard two-temperature model (TTM) is

$$C_e \frac{\partial T_e}{\partial t} = \nabla \cdot (k_e \nabla T_e) - G_{ep}(T_e - T_p) + S_e \quad \text{(A1)}$$

$$C_p \frac{\partial T_p}{\partial t} = \nabla \cdot (k_p \nabla T_p) + G_{ep}(T_e - T_p) + S_p \quad \text{(A2)}$$

Here T_e and T_p are the electron and phonon temperatures, C_e and C_p are volumetric heat capacities, k_e and k_p are thermal conductivities, G_{ep} is the electron–phonon coupling factor, and S_e and S_p are volumetric sources. The quantity D_p used to calibrate spatial phonon-energy transport is

$$D_p \equiv \frac{k_p}{C_p} \quad \text{(A3)}$$

D_p is the phonon thermal diffusivity.

For one spatial dimension, choose a reference time t_*, length L_*, and common temperature interval ΔT_*, and define $\theta_j = (T_j - T_{ref})/\Delta T_* (j = e, p)$, $\xi = t/t_*$, and $\zeta = x/L_*$. Equation (A2), with constant properties in the selected interval, become

$$\frac{\partial \theta_p}{\partial \xi} = Fo_p \frac{\partial^2 \theta_p}{\partial \zeta^2} + \Pi_{ep}(\theta_e - \theta_p) + Q_p \quad \text{(A4)}$$

$$\begin{cases} Fo_p = \frac{D_p t_*}{{L_*}^2} \\ \Pi_{ep} = \frac{G_{ep} t_*}{C_p} \\ Q_p = \frac{S_p t_*}{C_p \Delta T_*} \end{cases} \quad \text{(A5)}$$

$$Fo_e = \frac{D_e t_*}{{L_*}^2}, \ \Pi_{ee} = \frac{G_{ep} t_*}{C_e} \quad \text{(A6)}$$

The electron equation additionally contains Fo_e and Π_{ee} in Eq. (A6). Thus Fo_p measures spatial phonon diffusion during the imposed window, whereas Π_{ep} measures electron–phonon exchange during the same window.

APPENDIX B: LENGTH SCALING DETERMINES THE TIME AND VELOCITY RATIOS

After energy deposition, when the source and electron–phonon exchange are negligible over the spatial-redistribution window, Eq. (A4) is dominated by the phonon diffusion term. Balancing temporal and spatial variations give the phonon-energy diffusion time

$$t_{D,p} \sim \frac{{L_*}^2}{D_p} \quad \text{(B1)}$$

Here L_* is the actual length of the thermal disturbance or phase-change region. For comparing microscopic and macroscopic transport, a characteristic diffusion speed is defined by

$$u_{D,p} \equiv \frac{L_*}{t_{D,p}} = \frac{D_p}{L_*} \quad \text{(B2)}$$

This quantity is a length-time scale of Fourier diffusion. It must also be distinguished from the macroscopic scan speed V. With consistent definitions of L_* at the two scales, Eqs. (B1) and (B2) yield

$$R_t \equiv \frac{{t_{D,p}}^{mac}}{{t_{D,p}}^{mic}} = \frac{{D_p}^{mic}}{{D_p}^{mac}} \frac{{L_{mac}}^2}{L_{mic}} \quad \text{(B3)}$$

$$R_u \equiv \frac{{u_{D,p}}^{mic}}{{u_{D,p}}^{mac}} = \frac{{D_p}^{mic}}{{D_p}^{mac}} \frac{L_{mac}}{L_{mic}} = R_t \frac{L_{mic}}{L_{mac}} \quad \text{(B4)}$$

At fixed diffusivity, the diffusion time scales as the square of the length, whereas the characteristic diffusion speed scales inversely with the length.

In the crystalline phonon-gas approximation, the same quantities can be related to the phonon group velocity v_g and mean free path Λ_{ph} by

$$D_p = \frac{1}{3} v_g \Lambda_{ph} \quad \text{(B5)}$$

$$u_{D,p} = \frac{1}{3} v_g \frac{\Lambda_{ph}}{L_*} = \frac{1}{3} v_g Kn \quad \text{(B6)}$$

Here $Kn = \Lambda_{ph}/L_*$. Equations (B5) and (B6) are strictly valid only in the diffusive regime $Kn \ll 1$; otherwise, they provide only order-of-magnitude estimates of the relevant kinetic scales. In the following calculations, the simulation size can be increased to reduce Kn; when $Kn \ll 1$ is not strictly satisfied, the Fourier matching is used only as a conditional continuum-diffusion approximation.

APPENDIX C: INTERFACIAL ENERGY BALANCE DETERMINES PHASE-CHANGE TIMESCALES

Melting and subsequent solidification are represented by a moving interface s(t). When nucleation and interface kinetics are not rate limiting, interface motion is controlled by phonon heat conduction and latent heat. With a consistent normal direction n and the corresponding sign convention for $\dot{s}$, interfacial energy conservation gives

$$\mathcal{L}_v \dot{s} = [[-k_p \frac{\partial T_p}{\partial n}]]_s^l \quad \text{(C1)}$$

The brackets denote the solid-to-liquid jump of the phonon heat flux, and and $\mathcal{L}_v$ is the volumetric latent heat. For a one-phase Stefan problem, let α denote the phase that conducts the dominant heat flux and use $\left|\frac{\partial T_p}{\partial n}\right| \sim \Delta T_p/s$.

Taking magnitudes in Eq. (C1) gives

$$\begin{cases} \mathcal{L}_v \dot{s} \sim \frac{{k_p}^{(\alpha)} \Delta T_p}{s} \\ {St_p}^{(\alpha)} = \frac{{C_p}^{(\alpha)} \Delta T_p}{\mathcal{L}_v} \end{cases} \quad \text{(C2)}$$

$$s^2 \sim 2{D_p}^{(\alpha)} {St_p}^{(\alpha)} t \quad \text{(C3)}$$

Here ${St_p}^{(\alpha)}$ is the phonon Stefan number of the dominant conducting phase. Equation (C3) is the diffusive $s \propto \sqrt{t}$ law. Evaluating it at the characteristic phase-change length L_φ gives the phase-change time and characteristic interface speed

$$t_\varphi \sim \frac{{L_\varphi}^2}{{D_p}^{(\alpha)} {St_p}^{(\alpha)}} \quad \text{(C4)}$$

$$u_\varphi \equiv \frac{L_\varphi}{t_\varphi} \sim {St_p}^{(\alpha)} {u_{D,p}}^{(\alpha)} \quad \text{(C5)}$$

For one-phase melting with heat supplied through the liquid, α denotes the liquid; for one-phase solidification with heat extracted through the solid, α denotes the solid. A two-phase Stefan problem must retain both fluxes in Eq. (C1) and cannot arbitrarily use the properties of one phase. Equation (C5) connects interface motion to phonon-energy diffusion but does not equate u_φ with $u_{D,p}$.

Similarity of a diffusion-controlled interface trajectory requires matching Fo_p and the relevant ${St_p}^{(\alpha)}$, together with normalized geometry, initial interface position, boundary-temperature or heat-flux histories, and normalized source terms. If electron–phonon exchange remains significant during phase change, Fo_e, Π_{ep}, Π_{ee}, Q_e, and Q_p must also be matched.

For unchanged material parameters, full TTM similarity generally cannot be obtained by geometric and temporal rescaling alone. Matching Fo_p at the same D_p and matching Π_{ep} at fixed $\frac{G_{ep}}{C_p}$ impose, respectively,

$$\frac{t_{mic}}{t_{mac_{Fo_p}}} \sim \frac{{L_{mic}}^2}{L_{mac}} \quad \text{(C6)}$$

$$\frac{t_{mic}}{t_{mac_{\Pi_{ep}}}} = 1 \quad \text{(C7)}$$

These conditions are incompatible when $L_{mic} \neq L_{mac}$. The proposed correspondence is therefore conditional on a phonon-diffusion-controlled phase-change stage. A single value of $\frac{D_p}{L_*}$ or a single cooling rate cannot establish equivalence of the complete two-temperature history, melting or solidification path, nucleation, interface mobility, microstructure, or defect formation.

APPENDIX D: FOURIER-NUMBER SIMILARITY CONSTRAINS THE MD COOLING RATE

For local macroscopic SLM cooling, consider a quasi-steady temperature field $\widetilde{\mathrm{T}}(n - Vt)$ near the solidification front, where V is the scan speed and $G = |\partial \mathrm{T}/\partial n|$. For a common analysis interval ΔT_*, the material-point cooling rate T_{mac}, thermal length L_T, and imposed cooling window t_{mac} are

$$\dot{T}_{mac} \equiv |dT/dt| = GV \quad \text{(D1)}$$

$$L_T = \frac{\Delta T_*}{G}, t_{mac} = \frac{\Delta T_*}{GV} = \frac{L_T}{V} \quad \text{(D2)}$$

L_T is the length of the selected local temperature interval, not the melt-pool size, and t_{mac} is not the time for the entire melt pool to dissipate its heat. The corresponding macroscopic and MD phonon Fourier numbers are

$${Fo_p}^{mac} = \frac{{D_p}^{mac} t_{mac}}{{L_T}^2} = \frac{{D_p}^{mac} G}{V \Delta T_*} \quad \text{(D3)}$$

$$Fo_{MD} = \frac{{D_p}^{mic} t_{MD}}{{L_{MD}}^2} \quad \text{(D4)}$$

Local phonon-diffusion matching requires $Fo_{MD} = {Fo_p}^{mac}$, in addition to the geometric, boundary, and source conditions stated in Appendix C. The imposed MD window and cooling rate then follow without presupposing t_{MD}:

$$t_{MD} = {Fo_p}^{mac} \frac{{L_{MD}}^2}{{D_p}^{mic}}, \; T_{MD} = \frac{\Delta T_*}{t_{MD}} \quad \text{(D5)}$$

The macroscopic engineering inputs for this order-of-magnitude estimate are a temperature gradient of $2.65 \times 10^6 K/m$, a scanning speed of $1.36 m/s$, and a $50K$ solidification interval. Assuming local thermal equilibrium, we neglect the effects of melt-pool advection, solidification latent heat, and property variations within this interval, retaining only temperature diffusion by heat conduction. The macroscopic thermal diffusivity is then represented by the ratio of thermal conductivity to volumetric heat capacity. On this basis, the reported thermal diffusivity of pure Ti at its melting point, $9.5 mm^2/\mathrm{s}$, is used as the representative value [19-20]. It estimates only the magnitude of the conduction contribution; it is neither a pure phonon diffusivity nor a strict window-averaged effective diffusivity incorporating advection, latent heat, and temperature-dependent properties. A more realistic value can be calculated from measured or calibrated temperature-dependent thermal conductivity, density, and specific heat, followed by averaging over the actual solidification interval; latent heat can be included through an enthalpy or apparent-heat-capacity model. For melt pools with significant advection, the effective diffusivity can be calibrated by inverse fitting to high-fidelity CFD including Marangoni flow and latent heat, or to in situ thermal histories.

The microscopic inputs are $L_{MD} = 25nm$ and ${D_p}^{mic} = 9.466 \times 10^{-6}\ \mathrm{m}^2/\mathrm{s}$, the latter obtained from Eq. (A3) with $k_p = 22 W/(m \cdot K)$ and $C_p =$

$2.324 \times 10^6 J/(m^3 \cdot K)$. Equations (D1)–(D2) give $L_T \approx 18.9\mu m$, $\dot{T}_{mac} \approx 3.6 \times 10^6 K/s$, and $t_{mac} \approx 13.9\mu s$. Using ${D_{eff}}^{mac}$ for the macroscopic diffusivity in Eqs. (D3) and (D5), and denoting the resulting macroscopic Fourier number by ${Fo_{eff}}^{mac}$, gives

$$R_t = \frac{{D_p}^{mic}}{{D_{eff}}^{mac}} \left(\frac{L_T}{L_{MD}}\right)^2 = \frac{T_{MD}}{T_{mac}} \approx 5.7 \times 10^5 \qquad \text{(D6)}$$

The matched microscopic cooling rate is therefore of order 10^0 K/ps within this reduced conduction-only closure. This is a conditional macroscopic-effective/microscopic-phonon comparison; convective enhancement requires a separate effective closure.

[1] Z.-C. Fang, Z.-L. Wu, C.-G. Huang, C.-W. Wu, Review on residual stress in selective laser melting additive manufacturing of alloy parts, Opt. Laser Technol. 129, 106283 (2020).

[2] M. Strantza et al., Effect of the scanning strategy on the formation of residual stresses in additively manufactured Ti-6Al-4V, Addit. Manuf. 45, 102003. (2021).

[3] Z.-C. Fang, Z.-L. Wu, L. Zhao, C.-G. Huang, and C.-W. Wu, Effects of thermal cycling on residual stress in alloy parts via selective laser melting, Opt. Laser Eng. 180, 108277 (2024).

[4] L. Thijs, F. Verhaeghe, T. Craeghs, J. V. Humbeeck, and J.-P. Kruth, A study of the microstructural evolution during selective laser melting of Ti–6Al–4V, Acta Mater. 58, 3303–3312 (2010).

[5] J. Yang, H. Yu, J. Yin, M. Gao, Z. Wang, and X. Zeng, Formation and control of martensite in Ti-6Al-4V alloy produced by selective laser melting, Mater. Des. 108, 308–318 (2016).

[6] F. Schmeiser, E. Krohmer, N. Schell, E. Uhlmann, and W. Reimers, Internal stress evolution and subsurface phase transformation in titanium parts manufactured by laser powder bed fusion—An in situ x-ray diffraction study, Adv. Eng. Mater. 23, 2001502 (2021).

[7] C. Li, S. Mishra, E. Holbrook, C. Ezenwata, and A. Strachan, High strain rate deformation mechanisms in fcc alloys as a function of load triaxiality, Phys. Rev. Mater. 9, 113604 (2025).

[8] H. Wang et al., Introducing C phase in additively manufactured Ti-6Al-4V: A new oxygen-stabilized face-centred cubic solid solution with improved mechanical properties, Mater. Today 61, 11–21 (2022).

[9] Y. Qian, K. Josh, G. Christoph, T. Rachel, S. Amit, Y. Zhenzhong, and M. M. Andrew, In situ TEM observation of FCC Ti formation at elevated temperatures, Scr. Mater. 140, 9–12 (2017).

[10] J. Xiao and C. Deng, Ultimate strength of nanotwinned face-centered cubic metals, Phys. Rev. Lett. 125, 266101 (2020).

[11] D. Iabbaden, J. Amodeo, C. Fusco, F. Garrelie, and J.-P. Colombier, Molecular dynamics simulation of structural evolution in crystalline and amorphous CuZr alloys upon ultrafast laser irradiation, Phys. Rev. Mater. 6, 126001 (2022).

[12] Z.-C. Fang, Z.-L. Wu, C.-G. Huang, and C.-W. Wu, Micro-scale thermodynamic model of microstructure and stress evolution in parts via selective laser melting, J. Mater. Sci. 57, 11918–11933 (2022).

[13] S. Liu and Y. C. Shin, Additive manufacturing of Ti6Al4V alloy: A review, Mater. Des. 164, 107552 (2019).

[14] Z. Qun, G. Ya-Fang, and Y. Xin, Surface and orientation effects on stress-induced hcp-fcc phase transformation in Ti nanopillars, Appl. Surf. Sci. 509, 145234 (2020).

[15] W. Bingqiang, W. Wenqian, G. Mingyu, Y. Shuwei, N. Song, S. Min, and W. Jian, Influence of lowering basal stacking fault energy on twinning behaviours, Acta Mater. 245, 118637 (2023).

[16] A. Rida, S. I. Rao, and J. A. El-Awady, Characteristics of ⟨a⟩ screw dislocations and their slip on prismatic and pyramidal planes in pure α titanium from atomistic simulations, Materialia. 24, 101503 (2022).

[17] J. Geng, H. Zhang, Y. Mao, Y. Chen, N. Wang, Q. Zhao, Y. Kang, Z. Hou, and L. Zhu, Effects of basal-pyramidal dislocation lock on intergranular deformation incompatibility in near-α titanium alloy, Scr. Mater. 272, 117076 (2026).

[18] B. Li, Q. W. Zhang, and S. N. Mathaudhu, Basal-pyramidal dislocation lock in deformed magnesium, Scr. Mater. 134, 37 (2017).

[19] K. Zhou, H. P. Wang, J. Chang, and B. Wei, Experimental study of surface tension, specific heat and thermal diffusivity of liquid and solid titanium, Chem. Phys. Lett. 639, 105 (2015).

[20] C. F. Badini, T. Santero, M. Rosito, and E. Padovano, Laser powder bed fusion of pure titanium: Optimization of processing parameters by means of efficient volumetric energy density approach, Metals 14, 1357 (2024).